A magneto-elastic vector-play model including piezomagnetic behavior

Luiz Guilherme da Silva, Laurent Bernard, Mathieu Domenjoud, Laurent Daniel

Journal of Magnetism and Magnetic Materials 609 (2024) 172439

Contents lists available at ScienceDirect

Journal of Magnetism and Magnetic Materials

journal homepage: www.elsevier.com/locate/jmmm

Research article

A magneto-elastic vector-play model including piezomagnetic behavior

Luiz Guilherme da Silva [a,b,c,*], Laurent Bernard [c], Mathieu Domenjoud [a,b], Laurent Daniel [a,b]

[a] Université Paris-Saclay, CentraleSupélec, CNRS, Laboratoire de Génie Électrique et Électronique de Paris, 91192, Gif-sur-Yvette, France
[b] Sorbonne Université, CNRS, Laboratoire de Génie Électrique et Électronique de Paris, 75252, Paris, France
[c] GRUCAD/EEL/CTC, Federal University of Santa Catarina, Florianópolis 88040-900, Brazil

ARTICLE INFO

Keywords:
Magneto-mechanical coupling
Magnetic hysteresis
Thermodynamic analysis
Constitutive equations

ABSTRACT

The mechanical state strongly influences the magnetic response of ferromagnetic materials. In this paper, the effect of time-varying mechanical stresses on magnetic behavior is modeled by combining a vector-play model and a multiscale approach. The approach incorporates the influence of the crystallographic texture. The model is applied to a polycrystalline low-carbon steel (DC04). Uniaxial measurements are used to identify the dissipation parameters. The model is further validated under complex uniaxial magneto-elastic loading conditions, different from those used for parameter identification, including simultaneous variations of magnetic field and stress. To the best of our knowledge, the proposed approach is the first multiaxial magneto-elastic hysteresis model able to describe the response of a magnetic material to simultaneously varying magnetic field and stress and validated under such loading conditions.

1. Introduction

The magnetic behavior of ferromagnetic materials is very sensitive to the application of mechanical loadings. The magneto-elastic couplings have been characterized mainly under uniaxial static stress (e.g. [1–11]), and sometimes under multiaxial static stress (e.g. [12–15]). Moreover, experimental measurements under uniaxial dynamic stress [16–23] also show non-linear and hysteretic magnetic response. The sensitivity of the magnetic response to dynamic stress is known as piezomagnetic behavior, and can be used to design force sensors and actuators [24–26], as well as in non-destructive testing methods [27,28]. Most approaches for magneto-elastic hysteresis modeling require that either stress [9,29,30] or magnetic field [31,32] are maintained constant. However, ferromagnetic materials in electromagnetic devices are subjected to complex loading conditions, with simultaneous variations of the magnetic field and mechanical stress. A model including this intricate coupled behavior is required for accurate design of electromagnetic devices.

Recently, an energy-based vector-play hysteresis model was proposed to describe the effect of multiaxial magneto-elastic loading conditions on the magnetic response of magnetic materials [30,33]. The model relies on a thermodynamic approach, decomposing the magnetic field into reversible and irreversible parts. The reversible field is related to a thermodynamic reversible process, whereas the irreversible field defines the dissipation. Nevertheless, this approach is limited to magneto-elastic loadings with static stress. This work is an extension of this previous energy-based vector-play model to consider the influence of time-varying mechanical loadings. Inspired by the decomposition of the magnetic field, an irreversible stress is introduced, which captures the dissipation due to stress variations. Moreover, in order to describe the strong effect of crystallographic texture on piezomagnetic loops [19], the vector-play model is associated with a simplified texture multiscale approach [34]. Using material parameters identified from simple uniaxial measurements, the model is applied to describe the magnetic behavior under more complex uniaxial magneto-elastic configurations. The results are compared with measurements performed on low-carbon steel DC04. Lastly, the proposed approach is analyzed in terms of thermodynamic consistency, highlighting its strengths and limitations.

2. Modeling

The approach is based on a recently proposed model for magnetic hysteresis of ferromagnetic materials under magneto-elastic loadings [30]. To take into account texture effects, a simplified texture multiscale model (STMSM) for the reversible behavior [34] is used and combined with an energy-based hysteresis approach [35]. The

* Corresponding author at: Université Paris-Saclay, CentraleSupélec, CNRS, Laboratoire de Génie Électrique et Électronique de Paris, 91192, Gif-sur-Yvette, France.
E-mail address: luiz.dasilva@geeps.centralesupelec.fr (L.G. da Silva).

https://doi.org/10.1016/j.jmmm.2024.172439
Received 30 June 2024; Received in revised form 11 August 2024; Accepted 14 August 2024
Available online 20 August 2024

modeling can be split into reversible (anhysteretic) and irreversible (hysteretic) behavior.

2.1. Reversible behavior

To model the reversible behavior, three scales are considered: the domain scale (denoted by the index α), the grain scale (denoted by the index g), and the polycrystal (or macroscopic) scale. At the domain scale, the magnetization $\vec{M}_\alpha$ and magnetostriction strain tensor $\boldsymbol{\epsilon}_\alpha^{\ \mu}$ of a domain family α with orientation $\vec{\alpha}$ are written as:

$$\vec{M}_\alpha = M_s \vec{\alpha} \qquad \text{with} \qquad \vec{\alpha} = \sum_i \alpha_i \vec{e}_i \tag{1}$$

$$\boldsymbol{\epsilon}_\alpha^{\ \mu} = \frac{3}{2}\begin{bmatrix} \lambda_{100}\left(\alpha_1^2 - \frac{1}{3}\right) & \lambda_{111}\alpha_1\alpha_2 & \lambda_{111}\alpha_1\alpha_3 \\ \lambda_{111}\alpha_2\alpha_1 & \lambda_{100}\left(\alpha_2^2 - \frac{1}{3}\right) & \lambda_{111}\alpha_2\alpha_3 \\ \lambda_{111}\alpha_3\alpha_1 & \lambda_{111}\alpha_3\alpha_2 & \lambda_{100}\left(\alpha_3^2 - \frac{1}{3}\right) \end{bmatrix}, \tag{2}$$

expressed in the orthonormal vector basis $(\vec{e}_1, \vec{e}_2, \vec{e}_3)$ that defines the crystal coordinate system. M_s is the saturation magnetization. λ_{100} and λ_{111} are the magnetostriction constants. The free-energy density g_α at the domain scale is written as [36]:

$$g_\alpha = g_\alpha^{mag} + g_\alpha^{el} + g_\alpha^{an} \tag{3a}$$

$$g_\alpha^{mag} = -\mu_0 \vec{M}_\alpha \cdot \vec{H} \tag{3b}$$

$$g_\alpha^{el} = -\boldsymbol{\sigma} : \boldsymbol{\epsilon}_\alpha^{\ \mu} \tag{3c}$$

$$g_\alpha^{an} = K_1\left(\alpha_1^2\alpha_2^2 + \alpha_2^2\alpha_3^2 + \alpha_3^2\alpha_1^2\right) + K_2\,\alpha_1^2\alpha_2^2\alpha_3^2, \tag{3d}$$

with $\vec{H}$ the magnetic field, $\boldsymbol{\sigma}$ the second-order stress tensor, and μ_0 the vacuum permeability. K_1 and K_2 are the magneto-crystalline anisotropy constants. The operator : represents the double-dot product.

With the definition of g_α, the volume fraction of a domain family α is evaluated using a Boltzmann relation [37]:

$$p_\alpha = \frac{\exp\left(-A_s\, g_\alpha\right)}{\sum_\alpha \exp\left(-A_s\, g_\alpha\right)}, \tag{4}$$

with A_s a material parameter. At the grain scale, the magnetization $\vec{M}_g$ and magnetostriction strain $\boldsymbol{\epsilon}_g^{\ \mu}$ are evaluated by the weighted sum over all the possible domain orientations:

$$\vec{M}_g = \sum_\alpha p_\alpha \vec{M}_\alpha \quad \text{and} \quad \boldsymbol{\epsilon}_g^{\ \mu} = \sum_\alpha p_\alpha \boldsymbol{\epsilon}_\alpha^{\ \mu}. \tag{5}$$

The set of possible domain orientations is defined through the nodes of an icosphere (2562 orientations) [34]. The macroscopic magnetization $\vec{M}$ and magnetostriction strain $\boldsymbol{\epsilon}_g^{\ \mu}$ are then calculated by a volume average over all grains:

$$\vec{M} = \sum_g p_g \vec{M}_g \quad \text{and} \quad \boldsymbol{\epsilon}^{\ \mu} = \sum_g p_g \boldsymbol{\epsilon}_g^{\ \mu}, \tag{6}$$

with p_g the proportion of each grain.

2.2. Irreversible behavior under variable field and constant stress

In the energy-based model approach under constant mechanical loadings [30], the magnetic field $\vec{H}$ is decomposed into reversible $\vec{H}_{rev}$ and irreversible parts, with $\vec{H} = \vec{H}_{rev} + \vec{H}_{irr}$. The reversible field $\vec{H}_{rev}$ is related to a reversible thermodynamic process. The irreversible field $\vec{H}_{irr}$ is related to the dissipation process. The magnetization $\vec{M}$ and the magnetostriction strain $\boldsymbol{\epsilon}^{\mu}$ are given by the reversible model evaluated at the applied stress $\boldsymbol{\sigma}$ and reversible field $\vec{H}_{rev}$:

$$\vec{M}(\boldsymbol{\sigma}, \vec{H}_{rev}) \qquad \text{and} \qquad \boldsymbol{\epsilon}^{\mu}(\boldsymbol{\sigma}, \vec{H}_{rev}). \tag{7}$$

An approximate explicit solution of the energy-based model results in a vector-play approach. In this case, the reversible field $\vec{H}_{rev}$ is

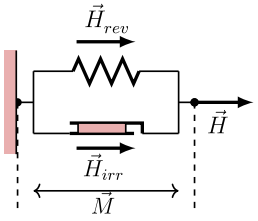

Fig. 1. Mechanical analogy of the magnetic hysteresis behavior.

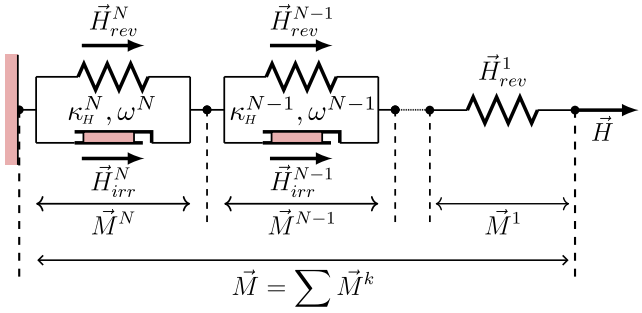

Fig. 2. Mechanical analogy of the magnetic hysteresis behavior considering N-cells.

updated at each time step by [35]:

$$\vec{H}_{rev} = \begin{cases} \vec{H}_{rev(p)} & \text{if } \|\vec{H} - \vec{H}_{rev(p)}\| \le \kappa_H \\ \vec{H} - \kappa_H \dfrac{\vec{H} - \vec{H}_{rev(p)}}{\|\vec{H} - \vec{H}_{rev(p)}\|} & \text{otherwise,} \end{cases} \tag{8}$$

with $\vec{H}_{rev(p)}$ the previous value of the reversible field, and κ_H the pinning field, which acts as a threshold and controls the irreversible process. The energy-based hysteresis model is formulated through an analogy of the magnetic hysteresis with a mechanical dry-friction system [35,38]. As illustrated in Fig. 1, irreversible behavior of magnetization $\vec{M}$ is allowed as the magnetic field $\vec{H}$ reaches the threshold – the pinning field κ_H – of the irreversible field $\vec{H}_{irr}$.

The modeling of the first magnetization curve, symmetric and asymmetric minor loops can be performed by considering a discrete distribution of pinning fields [35,39]. In this case, the weight ω^k of each pinning field is introduced and verifies:

$$\sum_{k=1}^{N} \omega^k = 1, \tag{9}$$

with N the total number of pinning fields. The reversible field update (8) in a multi-pinning fields context is given by:

$$\vec{H}_{rev}^{k} = \begin{cases} \vec{H}_{rev(p)}^{k} & \text{if } \|\vec{H} - \vec{H}_{rev(p)}^{k}\| \le \kappa_H^k \\ \vec{H} - \kappa_H^k \dfrac{\vec{H} - \vec{H}_{rev(p)}^{k}}{\|\vec{H} - \vec{H}_{rev(p)}^{k}\|} & \text{otherwise.} \end{cases} \tag{10}$$

Fig. 2 illustrates the mechanical analogy of the magnetic hysteresis. In this case, several dry-friction systems or cells are connected in series, driven by the same magnetic field. Each cell is characterized by a pinning field κ_H^k and a weight ω^k. The first cell (with $\kappa_H^k = 0$) represents the reversible bending of the Bloch walls [35].

The total magnetization $\vec{M}$ and magnetostriction strain $\boldsymbol{\epsilon}^{\mu}$ are evaluated from the weighted sum of each cell contribution:

$$\begin{aligned} \vec{M} &= \sum_{k=1}^{N} \omega^k \vec{M}^k \qquad \text{with} \qquad \vec{M}^k = M_{an}(\vec{H}_{rev}^{k}, \boldsymbol{\sigma}) \\ \boldsymbol{\epsilon}^{\mu} &= \sum_{k=1}^{N} \omega^k \boldsymbol{\epsilon}^{\mu,k} \qquad \text{with} \qquad \boldsymbol{\epsilon}^{\mu,k} = \epsilon_{an}^{\mu}(\vec{H}_{rev}^{k}, \boldsymbol{\sigma}), \end{aligned} \tag{11}$$

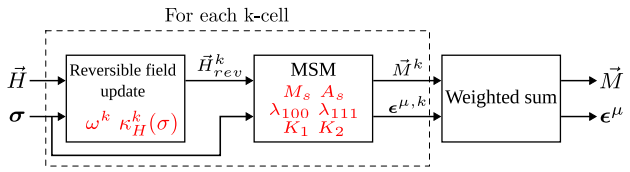

Fig. 3. Simplified schematic of the algorithm of the model under variations of field and constant stress. The material parameters are indicated in red.

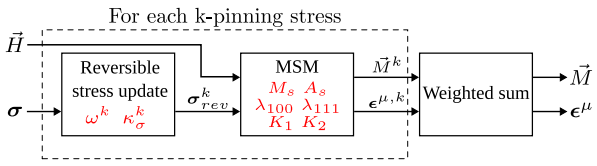

Fig. 4. Simplified schematic of the algorithm of the model under stress variations and constant field. The material parameters are indicated in red.

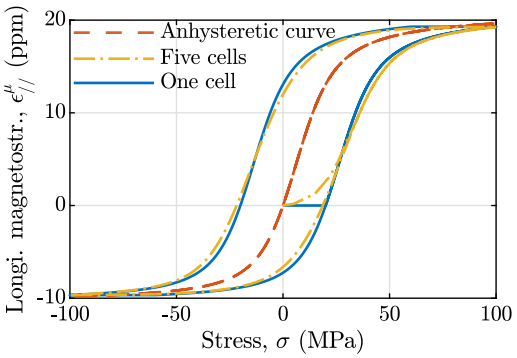

Fig. 5. Impact of a discrete distribution of pinning stresses on the strain–stress curve. Equivalent single-crystal isotropic material with parameters: $M_s = 1.71$ MA/m, $\lambda_s = 21$ ppm, $K_1 = K_2 = 0$. One cell parameters: $\kappa_\sigma = 20$ MPa, $\omega = 1$. Five cell parameters: $\kappa_\sigma = [0;\ 5;\ 15;\ 22;\ 26;\ 34]$ MPa, $\omega^k = [0.05;\ 0.1;\ 0.25;\ 0.25;\ 0.2;\ 0.15]$.

$\boldsymbol{M}_{an}$ and ϵ^{μ}_{an} are the anhysteretic magnetization and magnetostriction strain, respectively, evaluated from the multiscale approach.

The pinning fields distribution controls the coercive field of a hysteresis loop. To capture the stress effect in the coercive field, the following scaling of the pinning field is proposed [30]:

$$\kappa^k_H(\boldsymbol{\sigma}) = \kappa^k_H(\mathbf{0})\,\frac{H_c(\sigma_{eq})}{H_c(\mathbf{0})}, \tag{12}$$

with $\kappa^k_H(\mathbf{0})$ the pinning field for the stress-free case, $H_c(\mathbf{0})$ the stress-free coercive field and $H_c(\sigma_{eq})$ the coercive field under stress. σ_{eq} is an equivalent stress, defined by [40]:

$$\sigma_{eq} = \frac{3}{2}\vec{h}^t\left(\boldsymbol{\sigma} - \frac{1}{3}\,\mathrm{tr}(\boldsymbol{\sigma})\boldsymbol{I}\right)\vec{h}, \tag{13}$$

where $\vec{h}$ is a unit vector that defines the direction of $\vec{H}$, $\vec{h}^t$ is its transpose and $\mathrm{tr}(\boldsymbol{\sigma})$ is the trace of the stress tensor. σ_{eq} is a fictitious scalar stress which allows to capture – in a simplified manner – the effect of multiaxial stress on the magnetic behavior.

A schematic of the magneto-elastic vector-play model is presented in Fig. 3. In the first block, the reversible field is updated according to (10). Next, the reversible field $\vec{H}_{rev}$ and the stress $\boldsymbol{\sigma}$ serve as input of the multiscale approach. The magnetization $\vec{M}$ and magnetostriction strain $\boldsymbol{\epsilon}^{\mu}$ are the output of the model, and are solved at each loading step.

2.3. Irreversible behavior under variable stress and constant field

The modeling of the magnetic dissipation due to variations in mechanical loading and under static magnetic field is performed using a similar approach as presented in Section 2.2. In this case, the following mechanical decomposition is proposed:

$$\boldsymbol{\sigma} = \boldsymbol{\sigma}_{rev} + \boldsymbol{\sigma}_{irr}, \tag{14}$$

with $\boldsymbol{\sigma}_{rev}$ and $\boldsymbol{\sigma}_{irr}$ the reversible and irreversible stresses, respectively. Inspired from the vector-play approximation to the reversible field [35], an explicit update of the reversible stress is defined:

$$\boldsymbol{\sigma}_{rev} = \begin{cases} \boldsymbol{\sigma}_{rev(p)} & \text{if} \quad \|\boldsymbol{\sigma} - \boldsymbol{\sigma}_{rev(p)}\| \le \kappa_\sigma \\ \boldsymbol{\sigma} - \kappa_\sigma \dfrac{\boldsymbol{\sigma} - \boldsymbol{\sigma}_{rev(p)}}{\|\boldsymbol{\sigma} - \boldsymbol{\sigma}_{rev(p)}\|} & \text{otherwise,} \end{cases} \tag{15}$$

with κ_σ the pinning stress, and $\boldsymbol{\sigma}_{rev(p)}$ the previous value of the reversible stress. The norm operator of a second-order tensor $\boldsymbol{X}$ is evaluated by: $\|\boldsymbol{X}\| = \sqrt{\boldsymbol{X} : \boldsymbol{X}}$.

Following the same notion presented in Section 2.2, a discrete distribution of pinning stresses is introduced. Each cell is defined by a weight ω^k and a pinning stress κ^k_σ. In this situation with a distribution of pinning stresses, the explicit update of $\boldsymbol{\sigma}^k_{rev}$ is:

$$\boldsymbol{\sigma}^k_{rev} = \begin{cases} \boldsymbol{\sigma}^k_{rev(p)} & \text{if} \quad \|\boldsymbol{\sigma} - \boldsymbol{\sigma}^k_{rev(p)}\| \le \kappa^k_\sigma \\ \boldsymbol{\sigma} - \kappa^k_\sigma \dfrac{\boldsymbol{\sigma} - \boldsymbol{\sigma}^k_{rev(p)}}{\|\boldsymbol{\sigma} - \boldsymbol{\sigma}^k_{rev(p)}\|} & \text{otherwise.} \end{cases} \tag{16}$$

For each pinning stress κ^k_σ, a magnetization $\vec{M}^k$ and a magnetostriction strain $\boldsymbol{\epsilon}^{\mu,k}$ can be calculated. The total magnetization $\vec{M}$ and magnetostriction strain $\boldsymbol{\epsilon}^{\mu}$ are evaluated from a weighted sum of each contribution by:

$$\begin{aligned} \vec{M} &= \sum_{k=1}^{N} \omega^k \vec{M}^k \qquad \text{with} \qquad \vec{M}^k = M_{an}(\vec{H}, \boldsymbol{\sigma}^k_{rev}) \\ \boldsymbol{\epsilon}^{\mu} &= \sum_{k=1}^{N} \omega^k \boldsymbol{\epsilon}^{\mu,k} \qquad \text{with} \qquad \boldsymbol{\epsilon}^{\mu,k} = \epsilon^{\mu}_{an}(\vec{H}, \boldsymbol{\sigma}^k_{rev}). \end{aligned} \tag{17}$$

A simplified schematic of the approach is presented in Fig. 4. Under a constant magnetic field, the magnetic dissipation is only due to stress variations. The reversible stress $\boldsymbol{\sigma}^k_{rev}$ and the field $\vec{H}$ serve as input of the anhysteretic multiscale model. After the weighted sum operation of (17), the total magnetization $\vec{M}$ and magnetostriction $\boldsymbol{\epsilon}^{\mu}$ stress are updated at each time step.

To illustrate the influence of a distribution of pinning stresses on the magnetic behavior, consider the field-free case presented in Fig. 5, in which uniaxial stress is applied along longitudinal direction. For this simplified case, the macroscopic behavior is defined by a fictitious isotropic single crystal such that crystallographic texture effects are neglected. In the single cell example, the longitudinal component of the magnetostriction strain equals zero until the pinning stress ($\kappa_\sigma = 20$ MPa) is reached. Then, longitudinal magnetostriction variations occur, following the anhysteretic behavior shifted along the stress-axis.

Considering now a distribution of pinning stresses consisting of 3 cells ($N = 3$), the longitudinal magnetostriction strain gradually increases, following the thresholds defined by the pinning stresses, as shown in Fig. 5. It is also noted that by increasing the number of pinning stresses, the first magnetization curve can be refined. Such an analysis of the impact of the pinning stress on the magnetic response can also be made in the $B(\sigma)$ plane (piezomagnetic behavior).

2.4. Irreversible behavior under simultaneous variations of magnetic field and stress

In a more general case, in which variations in both field and stress are allowed, the magnetization $\vec{M}$ and magnetostriction strain

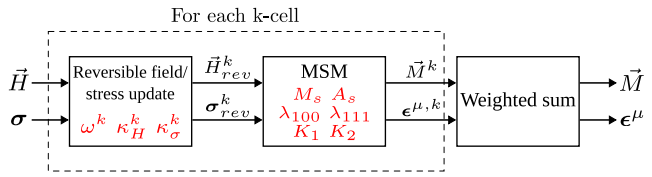

Fig. 6. Simplified schematic of the algorithm of the model. The material parameters are indicated in red.

ϵ^{μ} dependencies are written in terms of the reversible magnetic field $\vec{H}_{rev}$ and the reversible stress $\boldsymbol{\sigma}_{rev}$ by:

$$\vec{M}(\boldsymbol{\sigma}_{rev}, \vec{H}_{rev}) \quad \text{and} \quad \epsilon^{\mu}(\boldsymbol{\sigma}_{rev}, \vec{H}_{rev}). \tag{18}$$

In a multicell case, each cell is now characterized by a pinning stress κ_{σ}^{k}, a pinning field κ_{H}^{k}, and a weight ω^{k}. The same weight is applied for both magnetic and mechanical pinning parameters distributions, simplifying the modeling implementation and the hysteresis parameters identification.

The explicit update of reversible stress $\boldsymbol{\sigma}_{rev}^{k}$ is given by:

$$\boldsymbol{\sigma}_{rev}^{k} = \begin{cases} \boldsymbol{\sigma}_{rev(p)}^{k}, & \text{if } \|\boldsymbol{\sigma} - \boldsymbol{\sigma}_{rev(p)}^{k}\| \leq \kappa_{\sigma}^{k} |\operatorname{sign}(\|\dot{\boldsymbol{\sigma}}\|)| \\ \boldsymbol{\sigma} - \kappa_{\sigma}^{k} \dfrac{\boldsymbol{\sigma} - \boldsymbol{\sigma}_{rev(p)}^{k}}{\|\boldsymbol{\sigma} - \boldsymbol{\sigma}_{rev(p)}^{k}\|} |\operatorname{sign}(\|\dot{\boldsymbol{\sigma}}\|)|, & \text{otherwise,} \end{cases} \tag{19}$$

with $\dot{\boldsymbol{\sigma}}$ the time-derivative of the mechanical stress. The sign function is introduced such that it ensures a null irreversible stress – no dissipation – in the case of constant mechanical loading. Likewise, the explicit update of $\vec{H}_{rev}^{k}$ is given by:

$$\vec{H}_{rev}^{k} = \begin{cases} \vec{H}_{rev(p)}^{k}, & \text{if } \|\vec{H} - \vec{H}_{rev(p)}^{k}\| \leq \kappa_{H}^{k} |\operatorname{sign}(\|\dot{\vec{H}}\|)| \\ \vec{H} - \kappa_{H}^{k} \dfrac{\vec{H} - \vec{H}_{rev(p)}^{k}}{\|\vec{H} - \vec{H}_{rev(p)}^{k}\|} |\operatorname{sign}(\|\dot{\vec{H}}\|)|, & \text{otherwise,} \end{cases} \tag{20}$$

with $\dot{\vec{H}}$ the time-derivative of the magnetic field, and the sign function enforcing zero dissipation in the case of static field. The magnetization $\vec{M}$ and the magnetostriction strain ϵ^{μ} are evaluated by:

$$\begin{aligned} \vec{M} &= \sum_{k=1}^{N} \omega^{k} \vec{M}^{k} \quad \text{with} \quad \vec{M}^{k} = M_{an}(\vec{H}_{rev}^{k}, \boldsymbol{\sigma}_{rev}^{k}) \\ \epsilon^{\mu} &= \sum_{k=1}^{N} \omega^{k} \epsilon^{\mu,k} \quad \text{with} \quad \epsilon^{\mu,k} = \epsilon_{an}^{\mu}(\vec{H}_{rev}^{k}, \boldsymbol{\sigma}_{rev}^{k}). \end{aligned} \tag{21}$$

The schematic of the algorithm of the hysteresis model for a general magneto-elastic loading is shown in Fig. 6.

The main algorithm of the model is shown in Appendix A.

3. Experimental setup

The material studied in this work is a low-carbon steel DC04. The crystallographic texture for this material is obtained from electron back-scattering diffraction (EBSD) and is shown in Fig. 7 (gray scale). A set of 770 grain orientations is extracted from this measurement. It can be approximated by a perfect ⟨111⟩ fiber described by 16 grain orientations with equal proportions, as shown in Fig. 7 (blue markers).

The magneto-mechanical measurements are performed on the experimental setup shown in Fig. 8. A Zwick/Roell Z030 machine applies mechanical loading with the possibility to control force or displacement. A Teslameter FM302 and a transverse Hall probe 20 mT AS-VTP measure the magnetic field in the measurement area as shown in Fig. 8. From the Faraday–Lenz law, a voltage is induced in the B-coil, whose numerical integration results in the measured induction. The drift in induction is corrected by linear regression for each test. The

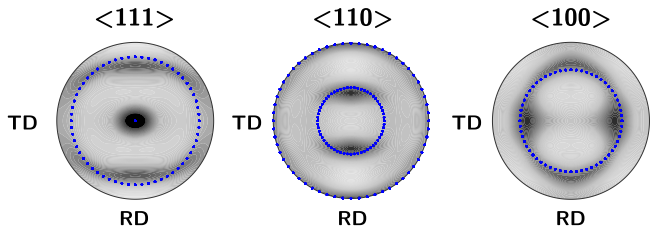

Fig. 7. Pole figures for a DC04 steel (stereographic projection) with 770 orientations (gray scale) superimposed with projections for a perfect ⟨111⟩ fiber with 16 orientations (blue markers).

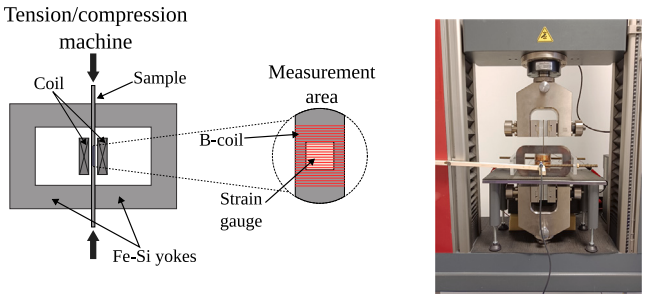

Fig. 8. Magneto-mechanical setup.

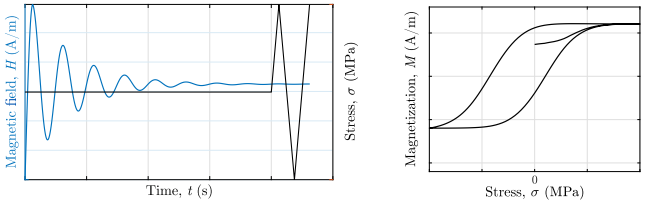

Fig. 9. Loading conditions in a piezomagnetic test (left) and an example of the corresponding piezomagnetic loop (right).

longitudinal and transverse magnetostriction strains are measured with a strain gauge rosette glued on the surface as shown in Fig. 8. More details on the experimental bench are presented in [41].

The piezomagnetic loops are measured as follows: the current is set as an exponentially decaying sine wave superimposed to a bias level, with frequency of 1 Hz. After stabilizing the current at the bias level, a cyclic force is applied with a speed of 0.5 mm/s and frequency of 11.5 mHz. Fig. 9 (left) summarizes the magneto-elastic loading conditions in a piezomagnetic test. After the mechanical cycle, the resulting piezomagnetic loop is illustrated in Fig. 9 (right). This test is repeated at several bias field levels. Considering several levels of bias field H_{dc}, the measured piezomagnetic loops are presented in Fig. 10 (top).

4. Identification of material parameters

4.1. Anhysteretic parameters

The anhysteretic material parameters for the single crystal are taken from pure iron and are listed in Table 1. The material parameter A_s can be identified from stress-free anhysteretic measurements [42]:

$$A_s = \frac{3\chi_0}{\mu_0 M_s^2}, \tag{22}$$

with χ_0 the initial susceptibility of a stress-free anhysteretic curve. A_s is identified as 5.5 10^{-3} J/m^3.

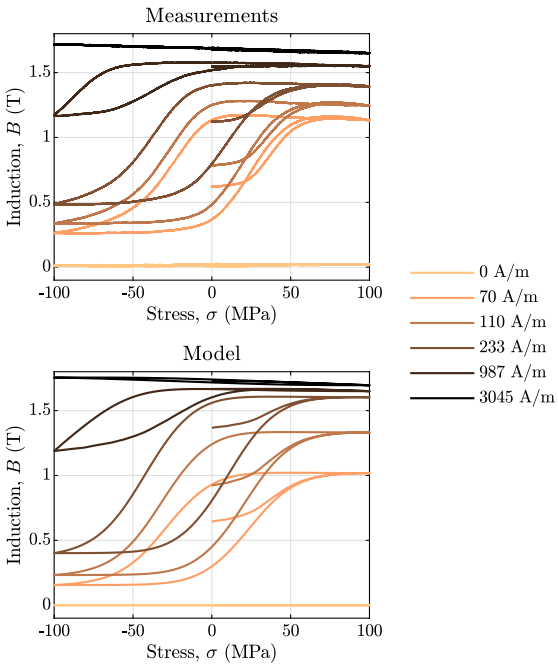

Fig. 10. Comparison between measured (top) and modeled (bottom) piezomagnetic curves under several levels of static field.

Table 1
Single crystal parameters for pure iron [43].

M_s (A/m)	λ_{100} (ppm)	λ_{111} (ppm)	K_1 (kJ/m^3)	K_2 (kJ/m^3)
1.71 10^6	21	−21	42.7	15

Table 2
Parameters related to the stress-dependence of κ_H^k [30].

a_1	a_2	a_3 (MPa^{-1})
1.25	1.2	0.04

4.2. Hysteresis model parameters identification from constant stress/variable field measurements

The dissipation parameters ω^k and κ_H^k can be identified from a set of measured coercive fields under increasing peak magnetic field for the stress-free magnetic case [44]. These parameters for DC04 are presented in [30], considering 16 pinning fields, and are given in Table 3. The determination of the total number of cells is detailed in Appendix B.

As observed in the measured hysteresis loops of Fig. 11 (top), a static stress modifies the coercive field. In order to model the mechanical loading influence on dissipation, as discussed in Section 2.2, an analytical function $a(\sigma_{eq})$ that shifts κ_H^k depending on the stress level is proposed in [30]. The parameters of $a(\sigma_{eq})$ are identified from a set of measured coercive fields under uniaxial stress. $a(\sigma_{eq})$ is here recalled:

$$\frac{H_c(\boldsymbol{\sigma})}{H_c(\mathbf{0})} = a(\sigma_{eq}) = a_1 \exp\left(-\exp(a_2 + a_3\sigma_{eq})\right) + 1, \tag{23}$$

with the three material parameters a_1, a_2 and a_3 listed in Table 2.

4.3. Hysteresis model parameters identification from constant field/variable stress measurements

The pinning stress distribution is identified using the procedure presented in [44,45] but applied to the case of time-varying mechanical loading. Starting from the demagnetized state, an uniaxial stress σ_a is applied. Considering a multicell case, the total reversible stress σ_{rev} is given by:

$$\sigma_{rev}(0 \to \sigma_a) = \int_0^\infty \omega(\kappa_\sigma) \max(\sigma_a - \kappa_\sigma, 0)\, d\kappa_\sigma = F(\sigma_a), \tag{24}$$

such that only the pinning stresses with $\kappa_\sigma < \sigma_a$ will be modified. An auxiliary function $F(\sigma)$ is then defined:

$$F(\sigma) = \int_0^\sigma \omega(\kappa_\sigma)(\sigma - \kappa_\sigma)\, d\kappa_\sigma, \tag{25}$$

with first and second derivatives given by:

$$\frac{\partial F}{\partial \sigma} = \int_0^\sigma \omega(\kappa_\sigma)\, d\kappa_\sigma, \qquad \frac{\partial^2 F}{\partial \sigma^2} = \omega(\sigma). \tag{26}$$

Following [44,45] but applying the method to the piezomagnetic case, the identification of $F(\sigma)$ is performed using a set of coercive stresses σ_c under increasing peak stress σ_{peak}. This set should be obtained from a measured field-free magnetostriction loop under variable stress. The saturation magnetostriction for DC04 is about 5.5 10^{-6} [30], and considering a Young modulus of about 192 GPa, a tension of 1 MPa produces an elastic strain similar, in magnitude, to the saturation magnetostriction. Therefore, the elastic strain hides the magnetostriction when stress is varying, so that magnetostriction strain versus stress measurements could not be performed. However, κ_σ^k can be identified from piezomagnetic measurements. In this case, the coercive stress σ_c is defined from each piezomagnetic loop using the stress values σ_c^+ and σ_c^- (such that $\sigma_c^+ > \sigma_c^-$) for which $B = B_{dc}$, with B_{dc} the bias level of induction (see Fig. 12 (top)). σ_c is given by:

$$\sigma_c = \frac{1}{2}\left(\sigma_c^+ - \sigma_c^-\right). \tag{27}$$

As the measured induction is close to zero under $H_{dc} = 0$ A/m in a piezomagnetic test (see Fig. 10), the κ_σ^k parameter is identified from a level of static field that is close to zero, but for which the induction

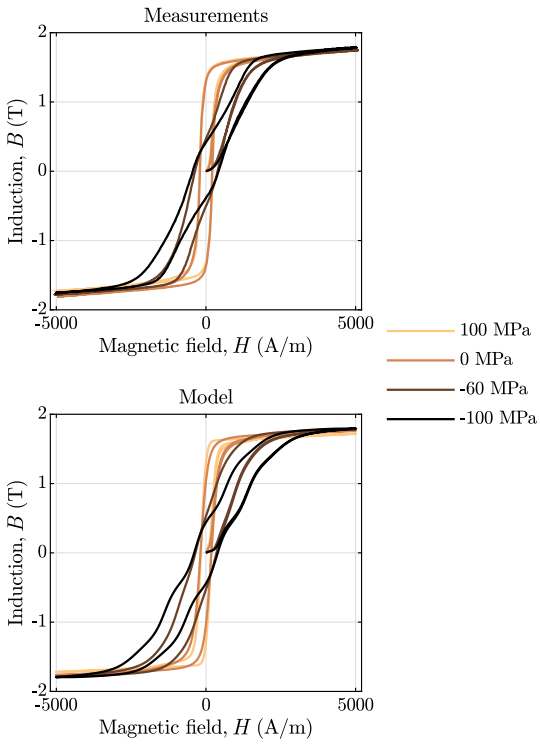

Fig. 11. Comparison between measured [30] (top) and modeled (bottom) magnetic hysteresis under several levels of static uniaxial stress.

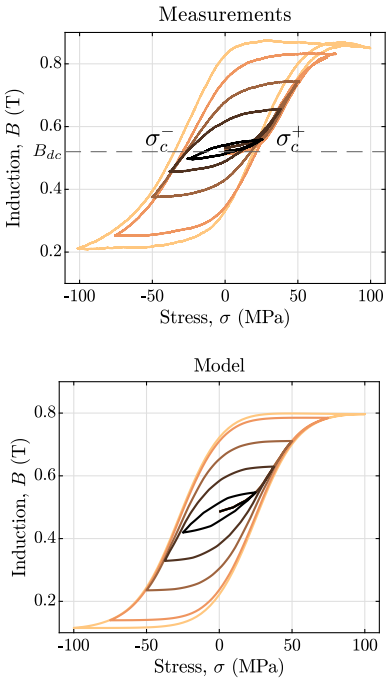

Fig. 12. Comparison between measured (top) and modeled (bottom) piezomagnetic loops under increasing peak stress and static field. The initial induction B_{dc} is about 0.51 T.

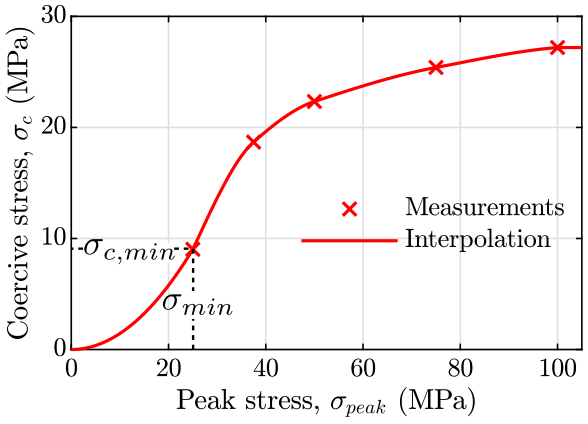

Fig. 13. Set of coercive stresses under increasing peak uniaxial stress and constant field $H_{dc} = 51$ A/m.

has a measurable value. The identification of κ_σ^k is performed from measurements under $H_{dc} = 51$ A/m. The piezomagnetic loops under increasing peak stress are depicted in Fig. 12 (top).

The set of coercive stresses under increments of mechanical loading is shown in Fig. 13. The coercive stress characteristic is quadratically extrapolated in the region of low mechanical loadings by:

$$\sigma_c(\sigma) = \sigma_{c,min}\left(\frac{\sigma}{\sigma_{min}}\right)^2, \qquad \text{if} \quad \sigma < \sigma_{min} \tag{28}$$

with $\sigma_{c,min}$ the minimum measured coercive stress corresponding to the peak stress σ_{min}. Using this set of coercive stresses, the identified auxiliary function $F(\sigma)$ is presented in Fig. 14.

The auxiliary function $F(\sigma)$ is interpolated by a smooth Spline function, allowing to evaluate the first and second derivatives by a

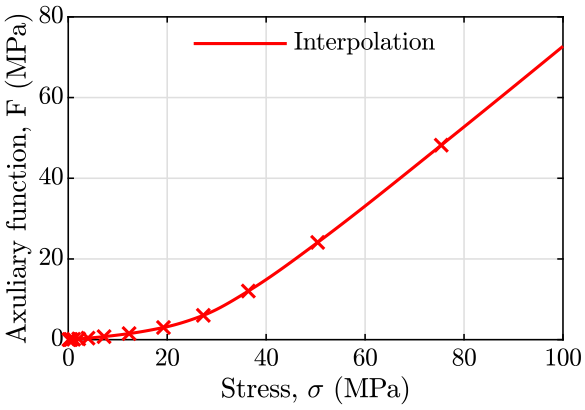

Fig. 14. Identified auxiliary function.

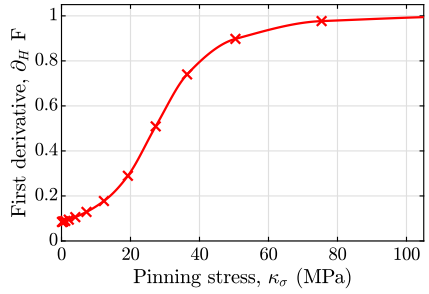

(a) First derivative

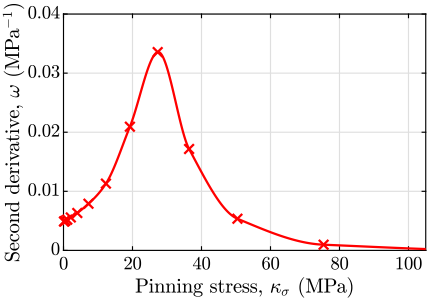

(b) Second derivative

Fig. 15. Derivatives of the auxiliary function $F(\sigma)$.

finite difference method detailed in [45]:

$$\frac{\partial F(x^j)}{\partial \sigma} \approx F(x^j)\frac{\Delta_2 - \Delta_1}{\Delta_1\Delta_2} + F(x^{j+1})\frac{\Delta_1}{\Delta_2\Delta_3} - F(x^{j-1})\frac{\Delta_2}{\Delta_1\Delta_3}$$
$$\frac{\partial F^2(x^j)}{\partial^2 \sigma} \approx 2\left(\frac{F(x^{j-1})}{\Delta_1\Delta_3} - \frac{F(x^j)}{\Delta_1\Delta_2} + \frac{F(x^{j+1})}{\Delta_2\Delta_3}\right) \tag{29}$$

with $\Delta_1 = x^j - x^{j-1}, \quad \Delta_2 = x^{j+1} - x^j, \quad \Delta_3 = x^{j+1} - x^{j-1}.$

The first and second derivatives of the auxiliary function $F(\sigma)$ are presented in Fig. 15. As observed in Fig. 15(a), the first derivative curve results in a cumulative distribution function (CDF). It can be noted from the CDF that all the pinning stresses are reached when an uniaxial loading above 100 MPa is applied. The second derivative of the auxiliary function (Fig. 15(b)) yields to the identified pinning stress probability density.

For numerical implementation, the continuous pinning stress distribution is discretized. Following [44], a set of points (x^k, y^k) is chosen to approximate the CDF curve. As illustrated in Fig. 16(a), a piece-wise linear function with $N = 16$ segments gives a good representation of the CDF. The discrete weight ω^k then corresponds to the area of a rectangle below the continuous distribution $\omega(\sigma)$, as presented in Fig. 16(b). Both

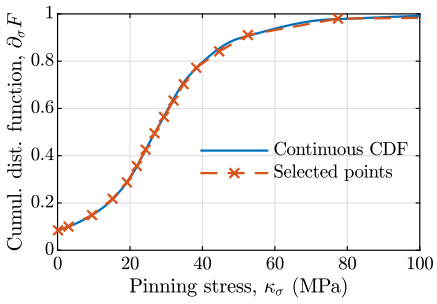

(a) Cumulative density distribution

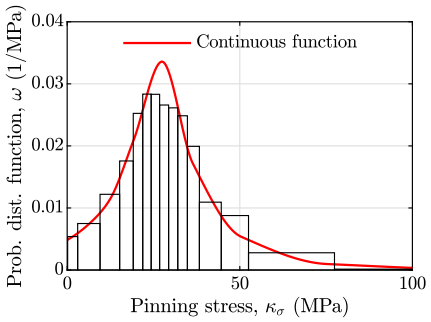

(b) Probability density distribution

Fig. 16. Discretization of the continuous pinning stress distribution.

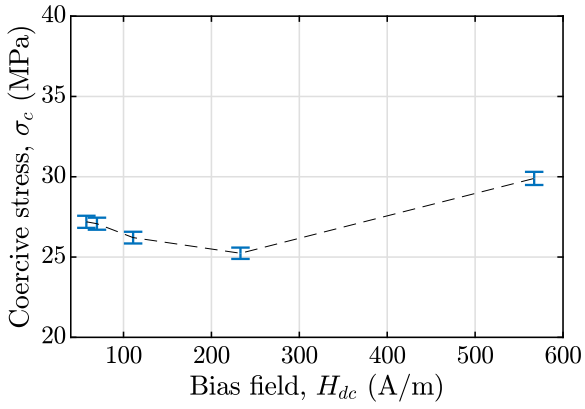

Fig. 17. Coercive stress characteristic under static field and a peak stress of 100 MPa.

weight ω^k and pinning stress κ^k are evaluated following [46]:

$$\omega^k = y^k - y^{k-1}$$
$$\kappa^k = \frac{(x^k y^k - F(x^k)) - (x^{k-1} y^{k-1} - F(x^{k-1}))}{\omega^k}. \quad (30)$$

The identified discrete pinning stresses are listed in Table 3.

The coercive stress depending on the level of static field H_{dc} is presented in Fig. 17 for the same peak stress of 100 MPa. The pinning stress κ_σ^k is considered constant under increments of static field in what follows.

5. Validation

5.1. Comparison of the model with anhysteretic measurements

The modeled anhysteretic magnetic response under uniaxial stress is presented in Fig. 18 (bottom). By considering a simplified crystallographic texture, the Villari reversal – in the region of about 2200 A/m – is captured by the model. Moreover, inflections (or bowing) under high compression are also captured, though the model overestimates this crystallographic texture effect, as observed in the case under −100 MPa.

Moreover, differences between the model and measurements are observed, especially at the knee of the anhysteretic curves. Discrepancies are attributed to two central factors: using a simplified texture (with 16 grains) instead of the full measured texture (with 770 grains), which allows the simulation time to be significantly reduced, and using single-crystal material parameters from pure iron.

The anhysteretic longitudinal magnetostriction strain under static uniaxial stress is shown in Fig. 19. These measurements are obtained from hysteresis tests, but here the longitudinal magnetostriction strain is presented as a function of magnetization, showing that the hysteresis effects are significantly reduced in the $\epsilon^\mu_{//}(M)$ representation compared to $\epsilon^\mu_{//}(H)$ (see Fig. 20). The rotation mechanism – depicted by the drop of magnetostriction at about 1.38 MA/m – is captured by the model. The model captures the trend of the longitudinal magnetostriction under uniaxial stress.

Table 3
Identified hysteresis parameters.

κ_H^k (A/m)	κ_σ^k (MPa)	ω^k
0	0	0.01
19.9	3.8	0.0693
87.7	5.0	0.0693
116.8	13.0	0.0693
133.1	18.2	0.0693
144.8	21.5	0.0693
153.3	23.6	0.0693
161.5	26.5	0.0693
170.9	28.6	0.0693
180.9	28.9	0.0693
190.6	31.1	0.0693
204.3	35.3	0.0693
228.1	37.8	0.0693
275.3	44.9	0.0693
439.4	56.0	0.0693
1454	75.8	0.02

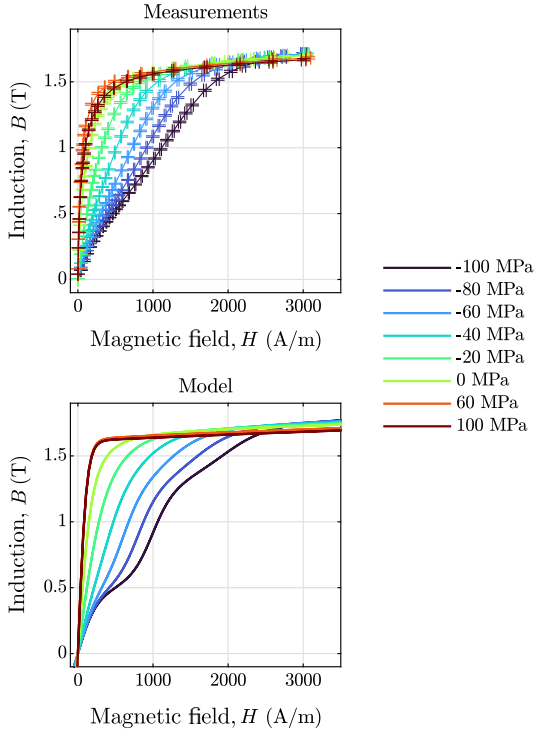

Fig. 18. Comparison between measured [30] and modeled anhysteretic magnetic behavior under several levels of static uniaxial stress.

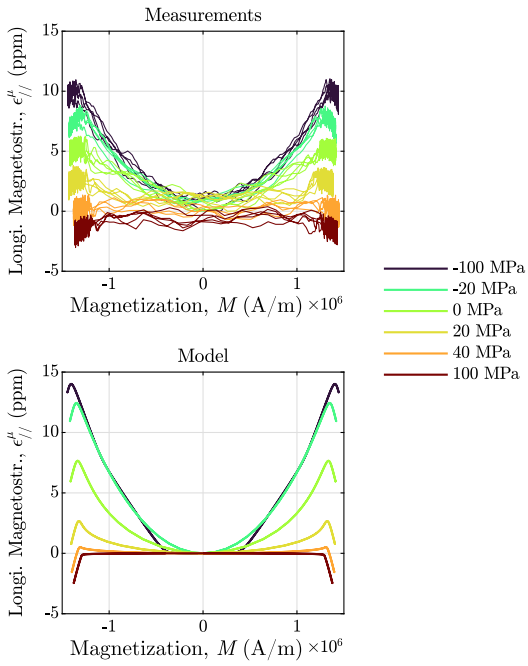

Fig. 19. Comparison between measured [30] and modeled anhysteretic magnetic behavior under several levels of static uniaxial stress.

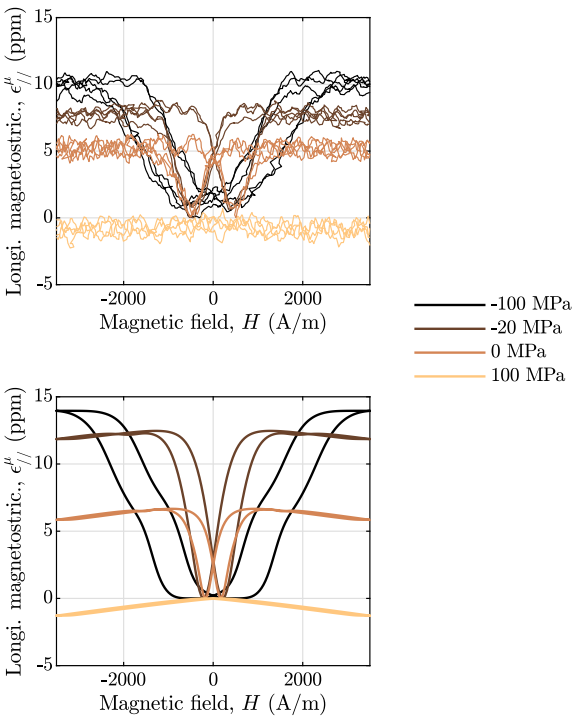

Fig. 20. Comparison between measured [30] (top) and modeled (bottom) longitudinal magnetostriction under static uniaxial stress.

5.2. Comparison of the model with hysteresis measurements

The magnetic hysteresis behavior under static stress is shown in Fig. 11. As presented in the anhysteretic modeling results, the texture effects, such as the Villari reversal and inflections under high compression, are also captured in the modeled magnetic hysteresis. Comparing these modeling results with those presented in [30], where an equivalent single-crystal was considered, the improvement by considering the simplified crystallographic texture is evident.

The modeled hysteretic behavior of longitudinal magnetostriction as a function of the magnetic field is presented in Fig. 20 (bottom). Under high field, it can be observed the formation of a small loop in the region related to the domain rotation, which corresponds to the drop in the magnetostriction strain presented in Fig. 19. This behavior does not characterize a dissipation (the area of the $\epsilon^{\mu}(H)$ loop is not an energy). The formation of the loop in the domain rotation region is not observable in the measurements due to the noise. The model overestimates the compression effect on longitudinal magnetostriction strain compared to the measurements (see Fig. 20 (top)). The modeling results can be improved if the measured crystallographic texture is used instead of the simplified one. Despite this drawback, Fig. 20 (bottom) highlights the modeling capabilities to capture the static uniaxial stress influence on the magnetostriction strain.

Applying a magneto-elastic loading of static field and quasi-static uniaxial stress, the model reproduces the measured symmetric minor loops (in terms of stress) by using the strategy of considering a discrete distribution of pinning stresses, as shown in Fig. 12 (bottom). Some differences are observed in the piezomagnetic loops under high tension, in which the model underestimates the increase in magnetization. One explanation is the use of a simplified crystallographic texture instead of the measured one. Fig. 21 (top) presents the piezomagnetic behavior under increasing stress considering the measured texture with 770 crystallographic orientations. Compared to the results with a simplified texture (see Fig. 21 (bottom)), a more significant increase in magnetization under tension is observed, which is consistent with the measurements (see Fig. 10 (top)). However, the simulation time is increased by about 22 times when considering 770 crystallographic

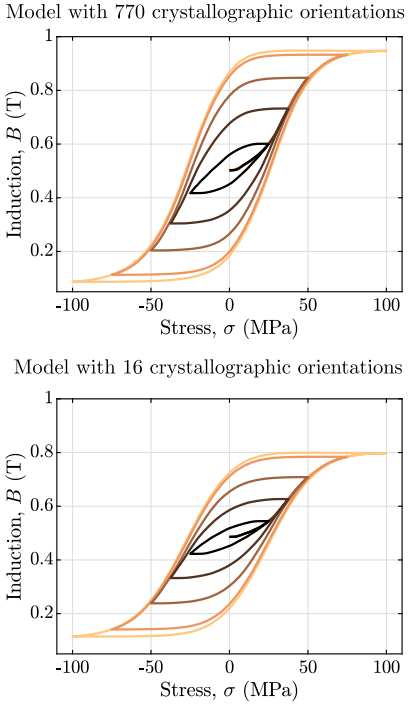

Fig. 21. Influence of the simplification of the crystallographic texture on the modeled piezomagnetic loops.

orientations. Keeping a reasonable simulation time, the simplified texture predicts the general trend of the piezomagnetic behavior under increasing stress.

Considering several levels of static field, the modeled piezomagnetic loops are depicted in Fig. 10. The Villari reversal is evident in the piezomagnetic loops with the slightly decreasing induction under high

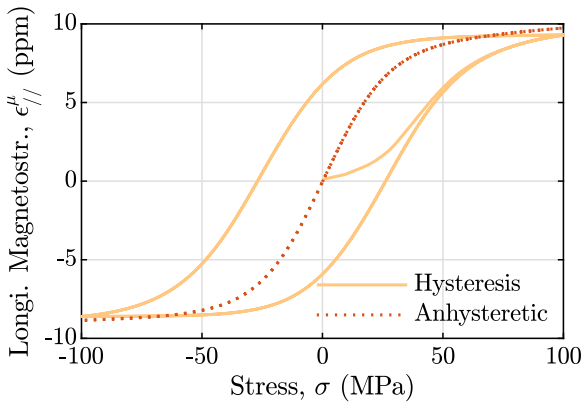

Fig. 22. Modeled mechanical behavior under quasi-static stress and zero static field.

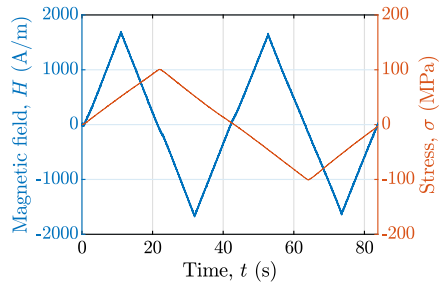

(a) Magneto-elastic loading

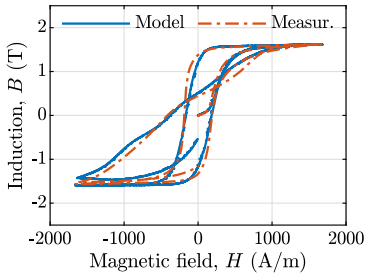

(b) Comparison of measured and modeled induction as a function of magnetic field

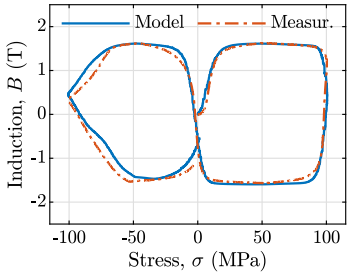

(c) Comparison of measured and modeled induction as a function of stress

Fig. 23. Magnetic response under simultaneous variations of field and stress.

tension. Such a texture-related behavior is captured by the model. The main differences are noted in the area of the loops (20% difference between modeled and measured results under H_{dc} = 233 A/m as the worst case). Despite this difference, the measured piezomagnetic trends under increasing bias field are captured by the model.

To illustrate the effect of mechanical dissipation, Fig. 22 shows the predicted longitudinal magnetostriction under varying stress and H_{dc} = 0 A/m. The mechanical dissipation is estimated as about 0.9 kJ/m^3 per cycle. As previously pointed out, the low magnetostriction strain of the tested material (DC04) did not allow the validation of the modeled magnetostriction under varying mechanical loadings. For comparison, the stress-free hysteresis losses in the case of time-varying magnetic field is about 1.5 kJ/m^3 per cycle.

A more complex validation configuration is when both the magnetic field and stress are varying in time. Considering the case of the magneto-elastic loading of Fig. 23(a), the magnetic response is shown as a function of the magnetic field in Fig. 23(b) and as a function of the stress in Fig. 23(c). A very good agreement is observed between modeling (blue solid lines) and experiments (red dashed lines).

6. Discussions on the model

To study the energetic consistency of the model, the case of variable stress and static magnetic field is analyzed first (for the case of static stress and varying field, the approach returns to the same thermodynamically consistent hysteresis model presented in [30,47]). In the case of varying stress and static magnetic field, the Clausius–Duhem inequality for the magneto-mechanical behavior is given by:

$$D = -\dot{\vec{H}} \cdot \vec{B} - \dot{\boldsymbol{\sigma}} : \boldsymbol{\epsilon} - \dot{g} \geq 0. \tag{31}$$

with $\boldsymbol{\epsilon}$ the strain. The magnetostriction strain $\boldsymbol{\epsilon}^{\mu}$ is introduced as internal variable to model the irreversible behavior due to stress variations. The internal variables are a modeling choice in a way that they unify in a single (or more) variable (or variables) the complex microscopic process that manifests in the form of dissipation at the macroscopic scale [48]. Taking into account the internal variable choice, the time-derivatives of the Gibbs free energy density $\dot{g}$ are given by:

$$\dot{g}(\boldsymbol{\sigma}, \vec{H}, \boldsymbol{\epsilon}^{\mu}) = \frac{\partial g}{\partial \boldsymbol{\sigma}} : \dot{\boldsymbol{\sigma}} + \frac{\partial g}{\partial \vec{H}} : \dot{\vec{H}} + \frac{\partial g}{\partial \boldsymbol{\epsilon}^{\mu}} : \dot{\boldsymbol{\epsilon}}^{\mu}. \tag{32}$$

Replacing (32) into (31), gives:

$$D = -\left[\boldsymbol{\epsilon} + \frac{\partial g}{\partial \boldsymbol{\sigma}}\right] : \dot{\boldsymbol{\sigma}} - \left[\vec{B} + \frac{\partial g}{\partial \vec{H}}\right] \cdot \dot{\vec{H}} - \frac{\partial g}{\partial \boldsymbol{\epsilon}^{\mu}} : \dot{\boldsymbol{\epsilon}}^{\mu} \geq 0. \tag{33}$$

From (33), the following relationships are defined, such that the restrictions of the second-law of thermodynamics are fulfilled:

$$\boldsymbol{\epsilon} = -\frac{\partial g}{\partial \boldsymbol{\sigma}}, \tag{34a}$$

$$\vec{B} = -\frac{\partial g}{\partial \vec{H}}, \tag{34b}$$

$$D = -\frac{\partial g}{\partial \boldsymbol{\epsilon}^{\mu}} : \dot{\boldsymbol{\epsilon}}^{\mu} \geq 0. \tag{34c}$$

To determine the irreversible behavior in terms of the internal variables, first, a dissipation function $\phi_d(\dot{\boldsymbol{\epsilon}}^{\mu})$ is introduced such that $\phi_d : \mathfrak{R}^n \rightarrow \mathfrak{R}$. The dissipation function can be non-smooth – or non-differentiable at some points – and per definition is characterized by [49]:

$$\frac{\partial \phi_d}{\partial \dot{\boldsymbol{\epsilon}}^{\mu}} = -\frac{\partial g}{\partial \boldsymbol{\epsilon}^{\mu}}. \tag{35}$$

The dissipation inequality can be written as:

$$D = \frac{\partial \phi_d}{\partial \dot{\boldsymbol{\epsilon}}^{\mu}} : \dot{\boldsymbol{\epsilon}}^{\mu} \geq 0, \tag{36}$$

and the following constraints in defining ϕ_d are necessary conditions to fulfill the restrictions of the second-law of thermodynamics:

$$\phi_d(\mathbf{0}) = 0 \qquad \text{and} \qquad \phi_d(\dot{\boldsymbol{\epsilon}}^{\mu}) \geq 0. \tag{37}$$

In the case of rate-independent dissipation functions, which is the interest here, ϕ_d is assumed to be positively homogeneous of degree one and therefore [49]:

$$\phi_d(\tau \dot{\boldsymbol{\epsilon}}^{\mu}) = \tau^k \phi_d(\dot{\boldsymbol{\epsilon}}^{\mu}) \quad \text{with} \quad \tau \in \mathfrak{R}_+ \quad \text{and} \quad k = 1. \tag{38}$$

Using the chain rule, the following relationship can be defined:

$$\frac{\partial \phi_d}{\partial \dot{\boldsymbol{\epsilon}}^{\mu}} : \dot{\boldsymbol{\epsilon}}^{\mu} = \phi_d(\dot{\boldsymbol{\epsilon}}^{\mu}). \tag{39}$$

Therefore, the dissipation function $\phi_d(\dot{\boldsymbol{\epsilon}}^{\mu})$ defines the evolution of dissipation D by:

$$D = \phi_d(\dot{\boldsymbol{\epsilon}}^{\mu}) \geq 0. \tag{40}$$

From (35), a minimization procedure can be established to evaluate the hysteresis behavior under variable mechanical loadings and static fields. In this case, the energy density g and the dissipation function ϕ_d need to be defined. Following the analogy of the magnetic hysteresis with a dry-friction mechanism [35,38], the dissipation function ϕ_d is defined as:

$$\phi_d(\dot{\boldsymbol{\epsilon}}^{\mu}) = \kappa_\sigma \|\dot{\boldsymbol{\epsilon}}^{\mu}\|, \tag{41}$$

with κ_σ a pinning stress. For small enough time-steps, the dissipation ϕ_d is approximated by:

$$\phi_d(\boldsymbol{\epsilon}^{\mu}) \approx \kappa_\sigma \frac{\|\boldsymbol{\epsilon}^{\mu} - \boldsymbol{\epsilon}^{\mu}_{(p)}\|}{\Delta t}, \tag{42}$$

with $\boldsymbol{\epsilon}^{\mu}_{(p)}$ the magnetostriction strain at the previous time-step. From this approximation, the partial derivative of the dissipation function ϕ_d is given by:

$$\frac{\partial \phi_d}{\partial \dot{\boldsymbol{\epsilon}}^{\mu}} \approx \frac{\partial \phi_d}{\partial \left(\dfrac{\boldsymbol{\epsilon}^{\mu} - \boldsymbol{\epsilon}^{\mu}_{(p)}}{\Delta t} \right)} = \Delta t \, \frac{\partial \phi_d}{\partial \boldsymbol{\epsilon}^{\mu}}. \tag{43}$$

From the definition of (35) and taking into account the approximation (43), the magnetostriction strain $\boldsymbol{\epsilon}^{\mu}$ is calculated from a minimization by:

$$\frac{\partial}{\partial \boldsymbol{\epsilon}^{\mu}} \left[g(\boldsymbol{\sigma}, \vec{H}, \boldsymbol{\epsilon}^{\mu}) + \Delta t \, \phi_d(\boldsymbol{\epsilon}^{\mu}) \right] = 0 \quad \rightarrow$$

$$\boldsymbol{\epsilon}^{\mu} = \arg\min \quad \left[g(\boldsymbol{\sigma}, \vec{H}, \boldsymbol{\epsilon}^{\mu}) + \kappa_\sigma \|\boldsymbol{\epsilon}^{\mu} - \boldsymbol{\epsilon}^{\mu}_{(p)}\| \right] \quad \text{subject to} \quad \mathrm{tr}(\boldsymbol{\epsilon}^{\mu}) = 0. \tag{44}$$

The energy density $g(\boldsymbol{\sigma}, \vec{H}, \boldsymbol{\epsilon}^{\mu})$ can be chosen as:

$$g(\boldsymbol{\sigma}, \vec{H}, \boldsymbol{\epsilon}^{\mu}) = f(\vec{H}, \boldsymbol{\epsilon}^{\mu}) - \mu_0 \frac{H^2}{2} - \frac{1}{2} \left(\mathcal{C}^{-1} \, \boldsymbol{\sigma} \right) : \boldsymbol{\sigma} - \boldsymbol{\epsilon}^{\mu} : \boldsymbol{\sigma}, \tag{45}$$

with $\mathcal{C}$ the stiffness tensor, and $f(\vec{H}, \boldsymbol{\epsilon}^{\mu})$ a free energy density that can be obtained from the partial numerical inversion of a magneto-elastic anhysteretic model — here the multiscale approach. The time-derivative $\dot{f}$ is:

$$\dot{f}(\vec{H}, \boldsymbol{\epsilon}^{\mu}) = \boldsymbol{\sigma}_{rev} : \dot{\boldsymbol{\epsilon}}^{\mu} - \mu_0 \vec{M} \cdot \dot{\vec{H}} \quad \text{with} \quad \frac{\partial f}{\partial \boldsymbol{\epsilon}^{\mu}} = \boldsymbol{\sigma}_{rev} \quad \text{and} \quad \frac{\partial f}{\partial \vec{H}} = -\mu_0 \vec{M}. \tag{46}$$

and the reversible stress $\boldsymbol{\sigma}_{rev}$ is introduced. With the choice of $g(\boldsymbol{\sigma}, \vec{H}, \vec{M})$, (34a) and (34b) become:

$$\begin{aligned} -\frac{\partial g}{\partial \vec{H}} &= \mu_0 \left(\vec{H} + \vec{M} \right) = \vec{B} \\ -\frac{\partial g}{\partial \boldsymbol{\sigma}} &= \mathcal{C}^{-1} \boldsymbol{\sigma} + \boldsymbol{\epsilon}^{\mu} = \boldsymbol{\epsilon}^{e} + \boldsymbol{\epsilon}^{\mu} = \boldsymbol{\epsilon}, \end{aligned} \tag{47}$$

supposing small strains, with $\boldsymbol{\epsilon}^{e}$ the elastic strain. From (34c):

$$-\frac{\partial g}{\partial \boldsymbol{\epsilon}^{\mu}} = -\frac{\partial f}{\partial \boldsymbol{\epsilon}^{\mu}} + \boldsymbol{\sigma} = -\boldsymbol{\sigma}_{rev} + \boldsymbol{\sigma} = \boldsymbol{\sigma}_{irr}, \tag{48}$$

and the irreversible stress $\boldsymbol{\sigma}_{irr}$ is introduced, defining the mechanical loading decomposition into reversible and irreversible parts $\boldsymbol{\sigma} = \boldsymbol{\sigma}_{rev} + \boldsymbol{\sigma}_{irr}$.

Combining (44) and (45), the magnetostriction strain is given by the minimization:

$$\boldsymbol{\epsilon}^{\mu} = \arg\min \quad \left[f(\vec{H}, \boldsymbol{\epsilon}^{\mu}) - \boldsymbol{\epsilon}^{\mu} : \boldsymbol{\sigma} + \kappa_\sigma \|\boldsymbol{\epsilon}^{\mu} - \boldsymbol{\epsilon}^{\mu}_{(p)}\| \right] \quad \text{subject to} \quad \mathrm{tr}(\boldsymbol{\epsilon}^{\mu}) = 0, \tag{49}$$

by considering that $\mathcal{C}$ does not depends on $\boldsymbol{\epsilon}^{\mu}$, the terms of (45) involving:

$$\left(\mathcal{C}^{-1} \, \boldsymbol{\sigma} \right) : \boldsymbol{\sigma} \quad \text{and} \quad \mu_0 \vec{H} \cdot \vec{H} \tag{50}$$

are constants, and can be neglected in evaluating $\boldsymbol{\epsilon}^{\mu}$.

As the dissipation $\phi_d(\boldsymbol{\epsilon}^{\mu})$ in non-differentiable at $\boldsymbol{\epsilon}^{\mu} = \boldsymbol{\epsilon}^{\mu}_{(p)}$, the subsequent set defines the subgradients of ϕ_d [50]:

$$\frac{\partial \phi_d(\boldsymbol{\epsilon}^{\mu})}{\partial \boldsymbol{\epsilon}^{\mu}} \in \begin{cases} \boldsymbol{\sigma}_{irr}, \|\boldsymbol{\sigma}_{irr}\| \leq \kappa_\sigma, & \text{if } \boldsymbol{\epsilon}^{\mu} = \boldsymbol{\epsilon}^{\mu}_{(p)} \\ \boldsymbol{\sigma}_{irr} = \kappa_\sigma \dfrac{\boldsymbol{\epsilon}^{\mu} - \boldsymbol{\epsilon}^{\mu}_{(p)}}{\|\boldsymbol{\epsilon}^{\mu} - \boldsymbol{\epsilon}^{\mu}_{(p)}\|}, & \text{otherwise.} \end{cases} \tag{51}$$

By applying the vector-play approximation, an explicit solution of the model is obtained, and the reversible stress updates are given by:

$$\boldsymbol{\sigma}_{rev} = \begin{cases} \boldsymbol{\sigma}_{rev(p)} & \text{if} \quad \|\boldsymbol{\sigma} - \boldsymbol{\sigma}_{rev(p)}\| \leq \kappa_\sigma \\ \boldsymbol{\sigma} - \kappa_\sigma \dfrac{\boldsymbol{\sigma} - \boldsymbol{\sigma}_{rev(p)}}{\|\boldsymbol{\sigma} - \boldsymbol{\sigma}_{rev(p)}\|} & \text{otherwise,} \end{cases} \tag{52}$$

returning the model presented in Section 2.3. Therefore, the proposed approach is thermodynamically consistent in the case of static magnetic fields and varying mechanical loadings. However, as pointed out in [50], where the vector-play approximation is shown to exhibit limitations in the case of 2D spiral magnetic fields, it is expected that the vector-play approximation for the stress also may show limitations when complex stress loadings are applied.

7. Conclusion

A magneto-elastic hysteresis model taking into account simultaneous time-variations of magnetic field and mechanical stress has been presented. The dissipation due to variations of mechanical loading is modeled from an analogy of the decomposition of the magnetic field – into reversible and irreversible parts – applied to the mechanical stress. In this case, irreversible stress describes the dissipative behavior due to mechanical loading variations. A pinning stress parameter is introduced and is identified from piezomagnetic measurements. The approach captures the piezomagnetic behavior, and validation under simultaneously varying stress and magnetic field is performed with satisfying agreement. The model can be summarized as two thermodynamically consistent models in the situation of static stress and varying field, and in the situation of static field and varying stress. The model allows for multiaxial magneto-elastic loadings, and could be applied in a complex application, such as under rotating stress and static field, for example, with thermodynamic consistency. The proposed approach is the first magneto-elastic hysteresis model validated under general magneto-elastic loadings, permitting the representation of the magnetic hysteresis under static stress and variable magnetic field, static field and variable stress, and simultaneously time variations of magnetic field and stress.

CRediT authorship contribution statement

Luiz Guilherme da Silva: Writing – original draft, Conceptualization, Methodology, Software. **Laurent Bernard:** Writing – review & editing, Conceptualization, Supervision. **Mathieu Domenjoud:** Writing – review & editing, Conceptualization. **Laurent Daniel:** Writing – review & editing, Conceptualization, Supervision.

Declaration of competing interest

The authors declare the following financial interests/personal relationships which may be considered as potential competing interests: Laurent Bernard reports financial support was provided by Coordination of Higher Education Personnel Improvement. If there are other authors, they declare that they have no known competing financial interests or personal relationships that could have appeared to influence the work reported in this paper.

Data availability

Data will be made available on request.

Acknowledgments

The authors gratefully acknowledge Prof. Anne-Laure Helbert (ICMMO, CNRS, Université Paris-Saclay) for providing the EBSD measurements. The work of Laurent Bernard was supported by the National Council for Scientific and Technological Development, Brazil — CNPq. This work was partially supported by Brazilian Federal Agency for Support and Evaluation of Postgraduate Education (CAPES)/ French Committee for the Evaluation of University and Scientific Cooperation with Brazil (COFECUB) under Project No. 88881.191763/2018-01.

Appendix A. Algorithm of the model

The main algorithm of the magneto-elastic hysteresis model is presented below (Algorithm 1). The anhysteretic behavior is evaluated from the subroutine MSM.

Algorithm 1: Magneto-elastic hysteresis model

Input: $\boldsymbol{\sigma}, \vec{H}$
Output: $\boldsymbol{\epsilon}^{\mu}, \vec{M}$
Rev. parameters: $A_s, M_s, \lambda_{100}, \lambda_{111}, K_1, K_2$
Irr. parameters: $\omega^k, \kappa_H^k, \kappa_\sigma^k$
for $k = 1 : N$ **do**
  if $\|\vec{H} - \vec{H}^k_{rev(p)}\| \leq \kappa_H^k$ **then**
    $\vec{H}^k_{rev} \leftarrow \vec{H}^k_{rev(p)}$
  else
    $$\vec{H}^k_{rev} \leftarrow \vec{H} - \kappa_H^k \left(\frac{\vec{H} - \vec{H}^k_{rev(p)}}{\|\vec{H} - \vec{H}^k_{rev(p)}\|} \right)$$
  end
  if $\|\boldsymbol{\sigma} - \boldsymbol{\sigma}^k_{rev(p)}\| \leq \kappa_\sigma^k$ **then**
    $\boldsymbol{\sigma}^k_{rev} \leftarrow \boldsymbol{\sigma}^k_{rev(p)}$
  else
    $$\boldsymbol{\sigma}^k_{rev} \leftarrow \boldsymbol{\sigma} - \boldsymbol{\sigma}^k_{rev(p)} \left(\frac{\boldsymbol{\sigma} - \boldsymbol{\sigma}^k_{rev(p)}}{\|\boldsymbol{\sigma} - \boldsymbol{\sigma}^k_{rev(p)}\|} \right)$$
  end
  $\vec{M}^k, \boldsymbol{\epsilon}^{\mu,k} \leftarrow \mathtt{MSM}(A_s, M_s, \lambda_{100}, \lambda_{111}, K_1, K_2, \vec{H}^k_{rev}, \boldsymbol{\sigma}^k_{rev})$
  $\vec{M} \leftarrow \left(\omega^k \vec{M}^k\right) + \vec{M}$
  $\boldsymbol{\epsilon}^{\mu} \leftarrow \left(\omega^k \boldsymbol{\epsilon}^{\mu,k}\right) + \boldsymbol{\epsilon}^{\mu}$
end

Appendix B. Definition of the number of cells

The number of cells is determined by comparing the modeling results with measurements of the stress-free hysteresis loop under variable magnetic field. Some illustrative cases are presented in Fig. 24 considering different number of cells.

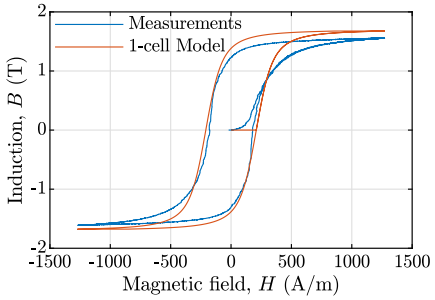

(a) Model with 1-cell

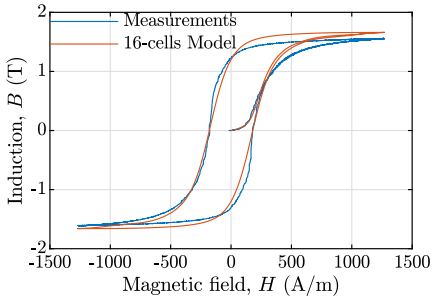

(b) Model with 16-cells

Fig. 24. Comparison between measurements and model for the stress-free magnetic hysteresis behavior.

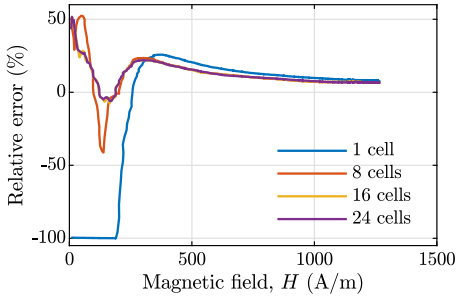

Fig. 25. Relative error between measurements and model.

The relative error between measurements and model is evaluated by:

$$error = \frac{B_{mod} - B_{mes}}{B_{mes}} \times 100, \tag{53}$$

with B_{mes} and B_{mod} the measured and modeled induction, respectively. The relative error considering the first magnetization curve for the stress-free case is presented in Fig. 25. Increasing the number of cells decreases the relative error, especially for low magnetic fields. However, above 16 cells, no significant modification is noted in the relative error, indicating that increasing the number of cells will only result in a higher computational cost.

References

[1] M. LoBue, C. Sasso, V. Basso, F. Fiorillo, G. Bertotti, Power losses and magnetization process in Fe–Si non-oriented steels under tensile and compressive stress, J. Magn. Magn. Mater. 215–216 (2000) 124–126, http://dx.doi.org/10.1016/S0304-8853(00)00092-5.

[2] K.J. Rizzo, O. Hubert, L. Daniel, Magnetic and magnetostrictive behavior of iron-silicon single crystals under uniaxial stress, IEEE Trans. Magn. 46 (2) (2010) 270–273, http://dx.doi.org/10.1109/TMAG.2009.2032146.

[3] D. Singh, F. Martin, P. Rasilo, A. Belahcen, Magnetomechanical model for hysteresis in electrical steel sheet, IEEE Trans. Magn. 52 (11) (2016) 1–9, http://dx.doi.org/10.1109/TMAG.2016.2590384.

[4] O. Perevertov, R. Schäfer, Magnetic properties and magnetic domain structure of grain-oriented Fe-3% Si steel under compression, Mater. Res. Express 3 (9) (2016) 1–12, http://dx.doi.org/10.1088/2053-1591/3/9/096103.

[5] N. Leuning, S. Steentjes, M. Schulte, W. Bleck, K. Hameyer, Effect of elastic and plastic tensile mechanical loading on the magnetic properties of NGO electrical steel, J. Magn. Magn. Mater. 417 (2016) 42–48, http://dx.doi.org/10.1016/j.jmmm.2016.05.049.

[6] H. Kawano, H. Oshima, J. Fujisaki, A. Furuya, Y. Uehara, T. Matsuo, Vector magnetic hysteresis measurement of nonoriented electrical steel sheets under unidirectional compressive stress applied by piezoelectric actuators, IEEE Trans. Magn. 53 (11) (2017) 1–8, http://dx.doi.org/10.1109/TMAG.2017.2703110.

[7] M.B. de Souza Dias, C. Bormio-Nunes, Stress annealing effect on the piezomagnetic coefficient of Fe–Al–B alloys, Phys. Lett. A 383 (9) (2019) 793–800, http://dx.doi.org/10.1016/j.physleta.2018.11.051.

[8] B.J. Mailhé, L.D. Bernard, L. Daniel, N. Sadowski, N.J. Batistela, Modified-SST for uniaxial characterization of electrical steel sheets under controlled induced voltage and constant stress, IEEE Trans. Instrum. Meas. 69 (12) (2020) 9756–9765, http://dx.doi.org/10.1109/TIM.2020.3006682.

[9] M.B. de Souza Dias, F.J.G. Landgraf, K. Chwastek, Modeling the effect of compressive stress on hysteresis loop of grain-oriented electrical steel, Energies 15 (3) (2022) 1–21, http://dx.doi.org/10.3390/en15031128, Art. no. 1128.

[10] M. Domenjoud, A. Pecheux, L. Daniel, Characterization and multiscale modeling of the magneto-elastic behavior of galfenol, IEEE Trans. Magn. 59 (11) (2023) 1–5, http://dx.doi.org/10.1109/TMAG.2023.3280925.

[11] G.M. Unniachanparambil, R. Rane, S.V. Kulkarni, Influence of compressive stress on the magnetic characteristics of grain-oriented material under non-sinusoidal excitation, J. Magn. Magn. Mater. 590 (2024) 171148, http://dx.doi.org/10.1016/j.jmmm.2023.171148.

[12] J. Pearson, P. Squire, M. Maylin, J. Gore, Biaxial stress effects on the magnetic properties of pure iron, IEEE Trans. Magn. 36 (5) (2000) 3251–3253, http://dx.doi.org/10.1109/20.908758.

[13] M. Rekik, O. Hubert, L. Daniel, Influence of a multiaxial stress on the reversible and irreversible magnetic behaviour of a 3% Si-Fe alloy, Int. J. Appl. Electromagn. Mech. 44 (3–4) (2014) 301–315, http://dx.doi.org/10.3233/JAE-141793.

[14] U. Aydin, P. Rasilo, F. Martin, A. Belahcen, L. Daniel, A. Haavisto, A. Arkkio, Effect of multi-axial stress on iron losses of electrical steel sheets, J. Magn. Magn. Mater. 469 (2019) 19–27, http://dx.doi.org/10.1016/j.jmmm.2018.08.003.

[15] O. Hubert, Z. Maazaz, J. Taurines, R. Crepinge, F. van den Berg, C. Celada-Casero, Influence of biaxial stress on magnetostriction—Experiments and modeling, J. Magn. Magn. Mater. (2023) 1–4, http://dx.doi.org/10.1016/j.jmmm.2023.170389, Art. no. 170389.

[16] D.J. Craik, M.J. Wood, Magnetization changes induced by stress in a constant applied field, J. Phys. D: Appl. Phys. 3 (7) (1970) 1009–1016, http://dx.doi.org/10.1088/0022-3727/3/7/303.

[17] K. Pitman, The influence of stress on ferromagnetic hysteresis, IEEE Trans. Magn. 26 (5) (1990) 1978–1980, http://dx.doi.org/10.1109/20.104589.

[18] X. Guo, D. Artherton, Magnetization changes in 2% Mn pipeline steel induced by uniaxial tensile stress cycles of increasing amplitude, IEEE Trans. Magn. 31 (5) (1995) 2510–2521, http://dx.doi.org/10.1109/20.406553.

[19] O. Hubert, K.J. Rizzo, Anhysteretic and dynamic piezomagnetic behavior of a low carbon steel, J. Magn. Magn. Mater. 320 (20) (2008) e979–e982, http://dx.doi.org/10.1016/j.jmmm.2008.04.082.

[20] P.G. Evans, M.J. Dapino, Measurement and modeling of magnetic hysteresis under field and stress application in iron–gallium alloys, J. Magn. Magn. Mater. 330 (2013) 37–48, http://dx.doi.org/10.1016/j.jmmm.2012.10.002.

[21] O. Ghibaudo, H. Chazal, N. Galopin, L. Garbuio, Magnetic coercive field measurement under ultrasonic mechanical excitation, Int. J. Appl. Electromagn. Mech. 48 (2–3) (2015) 207–212, http://dx.doi.org/10.3233/JAE-151989.

[22] D. Zhang, W. Huang, J. Zhang, W. Jin, Theoretical and experimental investigation on the magnetomechanical effect of steel bars subjected to cyclic load, J. Magn. Magn. Mater. 514 (2020) 167129, http://dx.doi.org/10.1016/j.jmmm.2020.167129.

[23] S. Bao, J. Yang, Y. Li, S. Bai, Research on the piezomagnetic hysteresis of ferromagnetic steels under elastic cyclic loadings with variable amplitudes, J. Magn. Magn. Mater. 568 (2023) 170373, http://dx.doi.org/10.1016/j.jmmm.2023.170373.

[24] S. Datta, J. Atulasimha, A. Flatau, Figures of merit of magnetostrictive single crystal iron–gallium alloys for actuator and sensor applications, J. Magn. Magn. Mater. 321 (24) (2009) 4017–4031, http://dx.doi.org/10.1016/j.jmmm.2009.07.067.

[25] L. Weng, T. Walker, Z. Deng, M. Dapino, B. Wang, Major and minor stress-magnetization loops in textured polycrystalline $Fe_{81.6}ga_{18.4}$ Galfenol, J. Appl. Phys. 113 (2) (2013) 1–9, http://dx.doi.org/10.1063/1.4772722, Art. no. 024508.

[26] V. Apicella, C.S. Clemente, D. Davino, D. Leone, C. Visone, Review of modeling and control of magnetostrictive actuators, Actuators 8 (2) (2019) http://dx.doi.org/10.3390/act8020045.

[27] P. Shi, S. Su, Z. Chen, Overview of researches on the nondestructive testing method of metal magnetic memory: Status and challenges, J. Nondestruct. Eval. 39 (2020) 1–37, http://dx.doi.org/10.1007/s10921-020-00688-z.

[28] M. Kashefi, L. Clapham, T.W. Krause, P.R. Underhill, A.K. Krause, Stress-induced self-magnetic flux leakage at stress concentration zone, IEEE Trans. Magn. 57 (10) (2021) 1–8, http://dx.doi.org/10.1109/TMAG.2021.3102822.

[29] T. Matsuo, Y. Takahashi, K. Fujiwara, Pinning field representation using play hysterons for stress-dependent domain-structure model, J. Magn. Magn. Mater. 499 (2020) 1–6, http://dx.doi.org/10.1016/j.jmmm.2019.166303, Art. no. 166303.

[30] L.G. da Silva, A. Abderahmane, M. Domenjoud, L. Bernard, L. Daniel, An extension of the vector-play model to the case of magneto-elastic loadings, IEEE Access 10 (2022) 126674–126686, http://dx.doi.org/10.1109/ACCESS.2022.3222833.

[31] K.J. Rizzo, O. Hubert, L. Daniel, A multiscale model for piezomagnetic behavior, Eur. J. Electr. Eng. 12 (4) (2009) 525–540.

[32] A. Ouaddi, O. Hubert, J. Furtado, D. Gary, S. Depeyre, Piezomagnetic behavior: Experimental observations and multiscale modeling, Mech. Ind. 20 (8) (2019) 810, http://dx.doi.org/10.1051/meca/2020050.

[33] L.G. da Silva, L. Bernard, F. Martin, A. Belahcen, L. Daniel, Multiaxial validation of a magneto-elastic vector-play model, IEEE Trans. Magn. 59 (11) (2023) 1–10, http://dx.doi.org/10.1109/TMAG.2023.3309154.

[34] L. Bernard, B.J. Mailhé, N. Sadowski, N.J. Batistela, L. Daniel, Multiscale approaches for magneto-elasticity in device simulation, J. Magn. Magn. Mater. 487 (2019) 1–13, http://dx.doi.org/10.1016/j.jmmm.2019.04.093, Art. no. 165241.

[35] F. Henrotte, A. Nicolet, K. Hameyer, An energy-based vector hysteresis model for ferromagnetic materials, COMPEL 25 (2006) 71–80, http://dx.doi.org/10.1108/03321640610634344.

[36] L. Daniel, N. Galopin, A constitutive law for magnetostrictive materials and its application to Terfenol-D single and polycrystals, Eur. Phys. J. Appl. Phys. 42 (2) (2008) 153–159, http://dx.doi.org/10.1051/epjap:2008031.

[37] N. Buiron, L. Hirsinger, R. Billardon, A multiscale model for magneto-elastic couplings, J. Physique IV 09 (1999) 187–196, http://dx.doi.org/10.1051/jp4:1999919.

[38] A. Bergqvist, Magnetic vector hysteresis model with dry friction-like pinning, Physica B 233 (4) (1997) 342–347, http://dx.doi.org/10.1016/S0921-4526(97)00319-0.

[39] V. François-Lavet, F. Henrotte, L. Stainier, L. Noels, C. Geuzaine, An energy-based variational model of ferromagnetic hysteresis for finite element computations, J. Comput. Appl. Math. 246 (2013) 243–250, http://dx.doi.org/10.1016/j.cam.2012.06.007.

[40] L. Daniel, O. Hubert, An equivalent stress for the influence of multiaxial stress on the magnetic behavior, J. Appl. Phys. 105 (7) (2009) 07A313, http://dx.doi.org/10.1063/1.3068646.

[41] M. Domenjoud, É. Berthelot, N. Galopin, R. Corcolle, Y. Bernard, L. Daniel, Characterization of giant magnetostrictive materials under static stress: Influence of loading boundary conditions, Smart Mater. Struct. 28 (9) (2019) 1–10, http://dx.doi.org/10.1088/1361-665X/ab313b, Art. no. 095012.

[42] L. Daniel, O. Hubert, N. Buiron, R. Billardon, Reversible magneto-elastic behavior: A multiscale approach, J. Mech. Phys. Solids 56 (3) (2008) 1018–1042, http://dx.doi.org/10.1016/j.jmps.2007.06.003.

[43] D. Jiles, Introduction to Magnetism and Magnetic Materials, Chapman and Hall, London, 1991.

[44] F. Henrotte, S. Steentjes, K. Hameyer, C. Geuzaine, Iron loss calculation in steel laminations at high frequencies, IEEE Trans. Magn. 50 (2) (2014) 333–336, http://dx.doi.org/10.1109/TMAG.2013.2282830.

[45] K. Jacques, S. Steentjes, H. François, C. Geuzaine, K. Hameyer, Representation of microstructural features and magnetic anisotropy of electrical steels in an energy-based vector hysteresis model, AIP Adv. 8 (4) (2018) 1–10, http://dx.doi.org/10.1063/1.4994199, Art. no. 047602.

[46] K. Jacques, Energy-Based Magnetic Hysteresis Models-Theoretical Development and Finite Element Formulations (Ph.D. thesis), Université de Liège, 2018.

[47] A. Sauseng, M. Kaltenbacher, K. Roppert, Revisiting the dry friction-like magnetic vector hysteresis model, J. Magn. Magn. Mater. 604 (2024) 172285, http://dx.doi.org/10.1016/j.jmmm.2024.172285.

[48] G.A. Maugin, The saga of internal variables of state in continuum thermo-mechanics (1893–2013), Mech. Res. Commun. 69 (2015) 79–86, http://dx.doi.org/10.1016/j.mechrescom.2015.06.009.

[49] C. Miehe, B. Kiefer, D. Rosato, An incremental variational formulation of dissipative magnetostriction at the macroscopic continuum level, Int. J. Solids Struct. 48 (13) (2011) 1846–1866, http://dx.doi.org/10.1016/j.ijsolstr.2011.02.011.

[50] L. Prigozhin, V. Sokolovsky, J.W. Barrett, S.E. Zirka, On the energy-based variational model for vector magnetic hysteresis, IEEE Trans. Magn. 52 (12) (2016) 1–11, http://dx.doi.org/10.1109/TMAG.2016.2599143.